

The properties of the X-ray corona in the distant ($z = 3.91$) quasar APM 08279+5255

E. Bertola^{1,2*}, C. Vignali^{1,2}, G. Lanzuisi², M. Dadina², M. Cappi², R. Gilli², G. A. Matzeu^{1,2,3}, G. Chartas⁴, E. Piconcelli⁵, and A. Comastri²

¹ Dipartimento di Fisica e Astronomia “Augusto Righi”, Università degli Studi di Bologna, via P. Gobetti 93/2, 40129 Bologna, Italy

² INAF–OAS, Osservatorio di Astrofisica e Scienza dello Spazio di Bologna, via P. Gobetti 93/3, 40129 Bologna, Italy

³ European Space Agency (ESA), European Space Astronomy Centre (ESAC), E-28691 Villanueva de la Cañada, Madrid, Spain

⁴ Department of Physics and Astronomy of the College of Charleston, Charleston, SC 29424, USA

⁵ INAF – Osservatorio Astronomico di Roma, Via Frascati 33, 00040 Monte Porzio Catone, Roma, Italy

Received ; accepted

ABSTRACT

We present new joint XMM-Newton and NuSTAR observations of APM 08279+5255, a gravitationally-lensed, broad-absorption line quasar ($z = 3.91$). After showing a fairly stable flux ($f_{2-10} \approx 4 - 5.5 \times 10^{-13} \text{ erg s}^{-1}$) from 2000 to 2008, APM 08279 was found in a fainter state in the latest X-ray exposures ($f_{2-10} \approx 2.7 \times 10^{-13} \text{ erg s}^{-1}$), which can likely be ascribed to a lower X-ray activity. Moreover, the 2019 data present a prominent Fe K α emission line and do not show any significant absorption line. This fainter state, coupled to the first hard X-ray sampling of APM 08279+5255, allowed us to measure X-ray reflection and the high-energy cutoff in this source for the first time. From the analysis of previous XMM-Newton and Chandra observations, X-ray reflection is demonstrated to be a long-lasting feature of this source, but less prominent prior to 2008, possibly due to a stronger primary emission. The estimated high-energy cutoff ($E_{\text{cut}} = 99^{+91}_{-35} \text{ keV}$) sets a new redshift record for the farthest ever measured and places APM 08279+5255 in the allowed region of the compactness-temperature diagram of X-ray coronae, in agreement with previous results on high- z quasars.

Key words. accretion, accretion disks – black hole physics – quasars: individual: APM 08279+5255 – quasars: absorption lines – quasars: supermassive black holes – X-rays: general

1. Introduction

Observational efforts in the past three decades have demonstrated the validity of the two-phase model (Haardt & Maraschi 1991; Haardt et al. 1994) in describing the high-energy emission of Active Galactic Nuclei (AGN). Optical/UV disc photons are predicted to be Compton up-scattered by the electrons of the hot corona ($T_e \sim 10^{8-9} \text{ K}$), which surrounds the central supermassive black hole (SMBH). The “Comptonization” process generates the cutoff-power-law-like spectrum measured in the X-rays, in which the cutoff energy is set by the temperature of the hot corona. At very hard energies, photon-photon collisions decay into electron-positron pairs which can, in turn, annihilate and produce energetic photons. Pair production can then become a runaway process acting as a natural thermostat for the corona. The conditions in which this takes place depend on a combination of corona temperature and radiative compactness (Cavaliere & Morrison 1980), as well as on the plasma optical depth (τ). In fact, Comptonization models of hot coronae with slab geometry predict a cutoff in the X-ray power law at $E_{\text{cut}}/k_B T_e \approx 2(3)$ for optically thin(thick) plasma (e.g., Petrucci et al. 2001). The typically employed quantities (Cavaliere & Morrison 1980; Guilbert et al. 1983) include the dimensionless temperature parameter:

$$\theta = \frac{k_B T_e}{m_e c^2} = \frac{E_{\text{cut}}}{K m_e c^2}, \quad (1)$$

with $K = 2(3)$ for an optically thin(thick) plasma, along with the dimensionless compactness parameter:

$$\ell = \frac{L_X}{R_X} \frac{\sigma_T}{m_e c^3}, \quad (2)$$

where m_e and T_e are electron mass and temperature, respectively, L_X and R_X are the luminosity and size of the X-ray source, respectively, σ_T is the Thomson scattering cross-section, and k_B is the Boltzmann constant.

In principle, by populating the $\ell - \theta$ diagram, it is possible to probe the mechanisms regulating the corona temperature and test the pair-production thermostat predictions. To that aim, broadband X-ray spectra of compact sources are needed to properly model the primary emission and, in particular, its high-energy cutoff. This was extensively done with hard X-ray observatories, such as *BeppoSAX* (e.g., Petrucci et al. 2001; Dadina 2007, 2008), *INTEGRAL* (e.g., Malizia et al. 2014), and *Swift* (e.g., Vasudevan et al. 2013; Koss et al. 2017). A real breakthrough in the study of X-ray coronae has arrived thanks to *NuSTAR* (Harrison et al. 2013), the first focusing hard X-ray telescope, which allowed for an improved estimation of the coronal temperature in nearby sources. By gathering literature results from both non-focusing instruments and *NuSTAR*, Fabian et al. (2015) built a compilation of E_{cut} measurements in both local AGN and black-hole binaries, finding many of their coronae to lie at the edge of the runaway pair-production region in the $\ell - \theta$ plane. Similar results were later obtained by Ricci et al. (2018) based on sources of the *Swift*/BAT AGN Spectroscopic Survey (BASS, Ricci et al.

* elena.bertola2@unibo.it

Table 1: Log of APM 08279+5255 observations from 2019

Observation	ObsID	Date	Net Exposure (ks)	f_{2-10}
XMM 101	0830480101	2019 <i>Mar</i> 24	24.1	$2.9^{+0.1}_{-0.3}$
Nu02	60401017002	2019 <i>Apr</i> 19	93.5 92.8	$2.8^{+0.2}_{-0.4}$ $3.2^{+0.3}_{-0.4}$
Nu04	60401017004	2019 <i>Apr</i> 22	59.7 59.2	$2.6^{+0.4}_{-0.4}$ $3.4^{+0.3}_{-0.6}$
XMM 301	0830480301	2019 <i>Apr</i> 23	24.5 28.2 25.7	$2.3^{+0.1}_{-0.2}$ $2.4^{+0.1}_{-0.3}$ $2.5^{+0.2}_{-0.3}$

Notes. Values of XMM 101 refer to EPIC-pn only; values of XMM 301 refer to EPIC-pn, -M1, -M2 respectively; values of *NuSTAR* refer to FPMA, FPMB, respectively. Observed-band 2–10 keV absorbed flux (10^{-13} erg cm $^{-2}$ s $^{-1}$, errors at 90% confidence level) is estimated using *acutpl* model. Net exposure: exposure time after cleaning the event file from flare events.

2017). Interestingly, Ricci et al. (2018) also discovered a negative correlation between the average high-energy cutoff and Eddington ratio in BASS AGN, regardless of either luminosity or SMBH-mass selection.

With its wide hard X-ray bandpass, *INTEGRAL* allowed for detailed studies of the coronal high-energy cutoff in local AGN (e.g., Molina et al. 2009, 2013; de Rosa et al. 2012), many of which were later updated and confirmed by *NuSTAR* measurements. Nonetheless, *NuSTAR* can properly constrain the high-energy cutoff only if this falls in its bandpass or, otherwise, only in high count-rate sources. The outstanding results obtained by *NuSTAR* have thus been restricted to nearby AGN ($z \lesssim 0.1$) with $E_{\text{cut}} \lesssim 200$ keV and $L_X \lesssim 10^{45}$ erg s $^{-1}$ (see, e.g., the recent work by Akylas & Georgantopoulos 2021), until recently, when Lanzuisi et al. (2019) (hereafter, L19) were able to probe the high-luminosity regime ($L_X > 2 \times 10^{45}$ erg s $^{-1}$) through *NuSTAR* observations of high- z AGN. L19 were the first to properly constrain the high-energy cutoff of two AGN at $z \gtrsim 2$ (2MASSJ1614346+470420 at $z = 1.86$ – hereafter, 2MASSJ16; B1422+231 at $z = 3.62$ – hereafter B1422) using *NuSTAR* data, confirming the measurement for B1422 by Dadina et al. (2016) from XMM-*Newton* data. Both sources show rather low E_{cut} values ($\lesssim 100$ keV) and fall in the limited allowed region for high-luminosity AGN of the $\ell - \theta$ plane. Interestingly, the measured E_{cut} values are much lower than those of BASS AGN showing similar Eddington ratios ($E_{\text{cut}} \sim 150 - 170$ keV, Ricci et al. 2018).

One of the most interesting high- z quasars is APM 08279+5255 ($z = 3.91$, APM 08279 hereafter; Irwin et al. 1989). This broad-absorption line quasar is lensed in three images by an as-yet-undetected foreground galaxy, possibly set at $z = 1.06$ (Ellison et al. 2004). Due to the lensing-system uncertainty, different models predict very different magnification values, ranging from $\mu_L = 4$ (Riechers et al. 2009) to $\mu_L = 100$ (Egami et al. 2000). Regardless of the actual magnification factor, APM 08279 is among the brightest high- z AGN in many bands, with one of the best sampled high- z spectral energy distributions (e.g., Stacey et al. 2018; Leung et al. 2019). In fact, APM 08279 is a very well known quasar in many astrophysical research fields and it lately became the first high- z quasar whose SMBH mass was estimated via reverberation mapping of the Si IV and C IV emission lines ($\log(M_{\text{BH}}/M_{\odot}) = 10 \pm 0.1$, Saturni et al. 2016). APM 08279 is also a very peculiar source for ultra-fast outflows (UFOs), namely, the X-ray winds that could be responsible for the generation of galaxy-wide outflows and thus for the establishment of the AGN-host-galaxy co-evolution (e.g., Faucher-Giguère & Quataert 2012; King & Pounds 2015; Costa et al. 2020). In fact, APM 08279 was the first high- z source in which UFOs were detected (Chartas et al. 2002) and it was later found to host some of the fastest X-ray winds ever seen (v_{out} up to

0.76 c , Chartas et al. 2009, hereafter C09). However, the most remarkable feature of APM 08279 is the double-velocity UFO present in all the observations up to early 2008 (C09; Saez et al. 2009), except for its first X-ray exposure (Hasinger et al. 2002, hereafter H02).

We present in this paper the first X-ray broadband analysis of APM 08279, making use of the latest XMM-*Newton* observations followed up by the first ever *NuSTAR* exposures of this source (2019, PI: G. Lanzuisi). The paper is organized as follows: reduction and analysis of 2019 observations are discussed in Sects. 2–3. Our results are then compared to previous *Chandra* and XMM-*Newton* observations, which we re-analyzed, in Sect. 4. We then place the observed X-ray corona properties in a broader context in Sect. 5. The scientific results are summarized in Sect. 6. We assume a flat Λ CDM cosmology (Planck Collaboration et al. 2020), with $H_0 = 70.0$ km s $^{-1}$ Mpc $^{-1}$ and $\Lambda_0 = 0.73$ throughout the paper.

2. Data reduction

APM 08279 was observed by XMM-*Newton* on 2019 *March* 24 for 31.4 ks (hereafter, XMM 101). On that date, EPIC-MOS cameras failed, thus it was observed again on 2019 *April* 23 for additional 33.3 ks (hereafter, XMM 301). These exposures were followed up by *NuSTAR* on 2019 *April* 19 for 93.5 ks (hereafter, Nu02) and on 2019 *April* 22 for 59.7 ks (hereafter, Nu04). The observation log is shown in Table 1.

XMM-*Newton* data were reduced applying standard procedure and the latest calibration files through SAS v.18.0. The event files of EPIC-pn cameras were filtered at 1.2 and 1.0 counts per second in the 10–12 keV band, for XMM 101 and 301, respectively, while those of XMM 301 EPIC-MOS cameras were filtered at 0.3 counts per second, in the same band. EPIC-pn source spectra were extracted from circular regions of 25'' radii for both XMM 101 and 301 ($\approx 80\%$ encircled energy fraction); EPIC-MOS source spectra were extracted using 20''-radius circles ($\approx 75\%$ encircled energy fraction). Background spectra were extracted from circular regions of 60'' radii for each XMM-*Newton* camera. Wider source regions, coupled with different good-time-interval filtering thresholds and other background extraction regions, were tested. No significant improvement of the spectral signal-to-noise ratio (S/N) was yielded, therefore, we stuck to the filtering and spectra extraction setup just described (i.e., source regions encircling the PSF core).

NuSTAR observations were processed using the standard pipeline of *NuSTAR* Data Analysis Software package (NuSTAR-DAS) v.2.0.0 (within Heasoft v.6.28) and calibrated with *NuSTAR* CALDB v.20200813. No significant background flares are present in these observations – a fact that we checked through

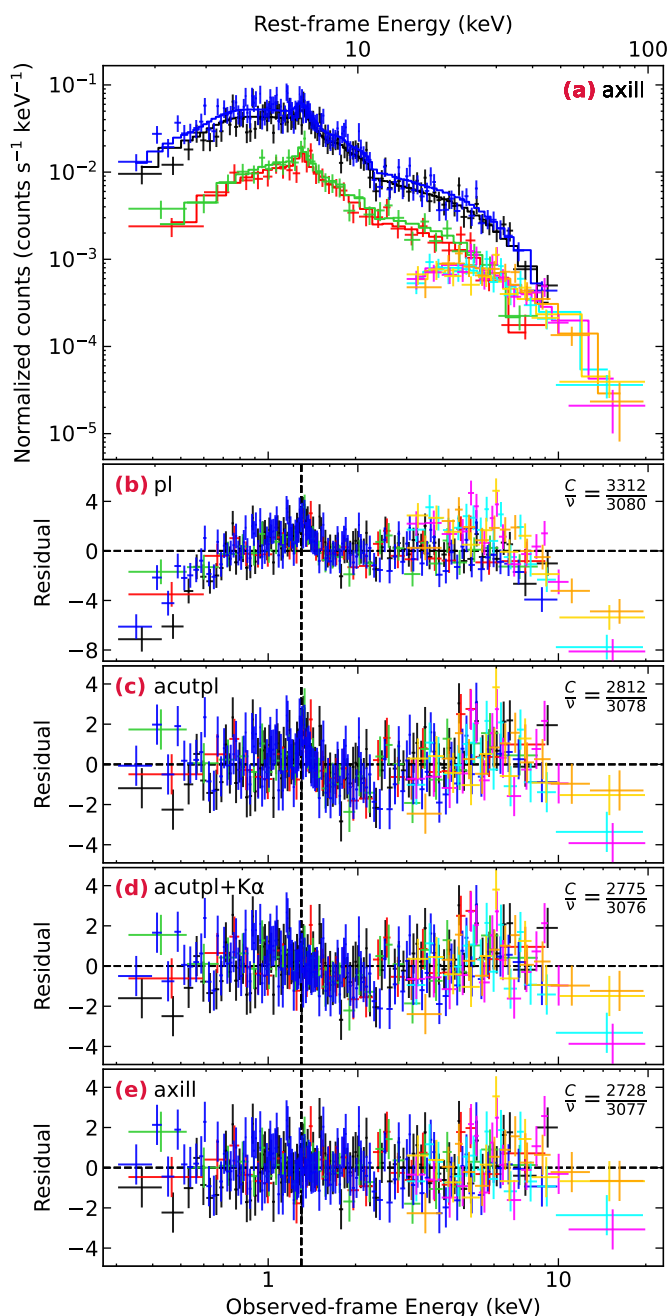


Fig. 1: Broadband X-ray spectra of APM 08279 collected by XMM-Newton and NuSTAR in 2019. Panel (a): Observed-frame spectra and best-fit model (axill model). Panels from (b) to (e): Observed-frame residuals. Vertical black dashed lines mark the energy of the Fe $K\alpha$ emission line. Spectra in each panel were rebinned to 4σ (with `setplot rebin 4 100` in Xspec) for showing purposes. Data are color-coded as follows: XMM 301 EPIC-pn is shown in black, XMM 301 EPIC-MOS1 in red, XMM 301 EPIC-MOS2 in green, XMM 101 EPIC-pn in blue, Nu02 FPMA in cyan and FPMB in magenta, Nu04 FPMA in yellow, and FPMB in orange. Model from top to bottom: (a) axill model, (b) pl model, (c) acutpl model, (d) acutpl+ $K\alpha$ model, (e) axill model. All models are modified by Galactic absorption ($N_{\text{H}} = 4.2 \times 10^{20} \text{ cm}^{-2}$). Best-fit parameters are summarized in Tables 2.

the IDL script `nustar_filter_lightcurve`¹. After testing different extraction regions to find the ones yielding the best S/N, we selected $40''$ -radius circles for the source ($\approx 60\%$ encircled energy fraction). These were coupled to annular background regions, centered on the target, with inner(outer) radii of $110''(170'')$ to exclude the wings of the source PSF and sample the non-uniform local background. This extraction setup was used for both FPMA and FPMB in each observation. Unfortunately, APM 08279 turned out to be fainter than expected based on past observations (as described in Sect. 4). Thus, during these exposures, source spectra are background dominated above $15 - 20 \text{ keV}$ regardless of the reduction and spectra-extraction setup.

3. Spectral analysis of 2019 data

Having checked that no significant intra-observation flux variability is present, we fit the time-averaged spectra with Xspec v.12.11.1. EPIC-pn data belong to the high-statistics regime, whereas EPIC-MOS and NuSTAR spectra to the mid-to-low-statistics regime (≈ 600 and 300 net counts, respectively). We grouped our data to 1 count/bin and applied C-statistics (Cash 1979) because matching the requirements to use the χ^2 statistics (at least 20 cts/bin) would have led to a loss in the energy resolution of NuSTAR and EPIC-MOS due to the coarse binning. Nevertheless, we also tested our models on spectra grouped at 20 cts/bin using χ^2 statistics as a sanity check and found results consistent to those presented here.

XMM 301 and the two NuSTAR observations are almost simultaneous, while XMM 101 was taken 30 days before XMM 301. No significant spectral variability is present between the two XMM-Newton epochs². Thus, we fit spectra from the four epochs together by linking all parameters, if not said otherwise, letting cross-calibration constants free to vary. Throughout the paper, all models are modified by Galactic absorption ($N_{\text{H}} = 4.2 \times 10^{20} \text{ cm}^{-2}$, HI4PI Collaboration et al. 2016) and errors and upper limits are given at 90% confidence level, unless otherwise stated.

3.1. Broadband X-ray spectra

The joint fit of XMM-Newton and NuSTAR data allows us to model the broadband-band continuum of APM 08279 in the $0.3 - 20 \text{ keV}$ observed-frame energy range (i.e., $\sim 1.5 - 98 \text{ keV}$ rest-frame energy range). The spectra present a cutoff at hard energies and soft absorption in excess of the Galactic value, which are clearly visible in the residuals against a single power-law model (pl Model; see Fig. 1, panel (b)). In fact, a `zphabs*zcutoffpl` model (hereafter, acutpl model; Fig. 1, panel (c)) well reproduces both features in statistical terms, but yields a power law that is considerably harder ($\Gamma \approx 1.3$) than expected values for an AGN (e.g., Vignali et al. 1999; Piconcelli et al. 2005; Just et al. 2007) and a very low high-energy cutoff ($E_{\text{cut}} \approx 34 \text{ keV}$). Absorption in the soft band is due to a “cold” medium placed at the systemic redshift of the source, with a column density consistent with previous observations (H02; C09). For the rest of the analysis, our models include this additional absorption component. The data clearly present a prominent Fe $K\alpha$ emission line, detected at $E_{\text{rest}} = 6.5 \pm 0.1 \text{ keV}$ ($E_{\text{obs}} \approx 1.3 \text{ keV}$) as a highly-

¹ <https://github.com/NuSTAR/nustar-idl>

² The ratio of the two EPIC-pn spectra shows no evident trend and is well consistent with being constant.

significant ($\Delta Cstat/\Delta\nu = 37/2$) narrow line³ on top of an acutpl continuum in both XMM-Newton observations. Therefore, we tie the Fe K α line component between the two epochs.

An acutpl+K α model fails to fit the high-energy bump (Fig. 1, panel (d)) which, combined with the low photon index and high Fe K α equivalent width (EW; rest-frame EW = 318^{+94}_{-90} eV) can be evidence for X-ray reflection. We tested this scenario through the non-relativistic reflection model *xillver*, part of the *relxill* package (García et al. 2014; Dauser et al. 2014), which accounts for a direct cutoff power law and its reprocessed emission (continuum and self-consistent emission and absorption features) by a distant, (possibly ionized) medium. Reflection is parameterized through photon index Γ ; high-energy cutoff, E_{cut} ; iron abundance (that we set to Solar); ionization of the disk, $\log \xi^4$; inclination angle, i ; and reflection fraction, R , defined as the fraction relative to the reflected emission expected from a slab subtending a 2π solid angle. Low inclination angles return a better fit and are naturally preferred by the data when the parameter is set free to vary; however, the data statistics prevents us from actually constraining it, thus we set $i = 30^\circ$. Similarly, we first leave the ionization of the disk free to vary and then freeze its value to its best fit ($\log(\xi/\text{erg s}^{-1} \text{cm}) = 1.7$). By the inclusion of the reflection continuum (axill model), we find a better representation of our broadband spectra, both statistically ($\Delta Cstat = 47$ for one additional parameter; see confidence contours in Fig. 2) and physically (see Table 2). The power-law photon index ($\Gamma = 2.1^{+0.1}_{-0.2}$) agrees with typical values of high- z sources (e.g., Vignali et al. 2005; Just et al. 2007) and so does the high-energy cutoff ($E_{cut} = 99^{+91}_{-35}$ keV) with the few other measurements available at $z > 1$ (Lanzuisi et al. 2016; Dadina et al. 2016; L19). The yielded reflection fraction ($R = 2.8^{+1.1}_{-0.9}$) carries the information that the reflecting material is seeing a source primary emission that is much larger than the one reaching the observer. Two of the possible explanations for such a large value of R are *i*) pc-scale reflection in which the primary source activity has dropped (and so has the direct emission seen by the observer), whereas the reflector is still illuminated by the echo of the previous stronger source emission due to the travel-time delay (e.g., Lanzuisi et al. 2016); *ii*) disc reflection in a lamp-post geometry where the corona height is low and thus light-bending is severe (e.g., Gandhi et al. 2007).

3.2. Search for UFO imprints

With its persistent double-velocity component X-ray wind (C09), APM 08279 is a one-of-a-kind object for studying UFOs in high- z AGN. However, 2019 data (see Fig. 1) appear not to show the prominent and broad features previously seen in this source. We thus searched our spectra only for narrow ($\sigma = 0.1$ keV, rest-frame) emission and absorption features. We applied the blind method of Miniutti & Fabian (2006), as implemented in Cappi et al. (2009), over the energy range spanned by past UFO events in APM 08279 ($E \approx 7 - 14$ keV) using the *axill* best fit as baseline model, also including the *NuSTAR* spectra to correctly model the broadband continuum. We then tested our

³ The line width is visually resolved, but letting this parameter free to vary yields no statistical improvement ($\Delta Cstat/\Delta\nu = 1/1$). Moreover, the best-fit line width is consistent with being narrow both based on its face value ($\sigma = 0.15$ keV) and its 90% confidence range ($\sigma < 0.7$ keV) in the rest frame. We thus set the rest-frame width of the Fe K α line to $\sigma = 0.1$ keV.

⁴ The ionization parameter ξ is defined as $\xi = L_X/nr^2$, where L_X is the X-ray luminosity of the incident radiation, n is the gas density and r is the distance from the ionizing source.

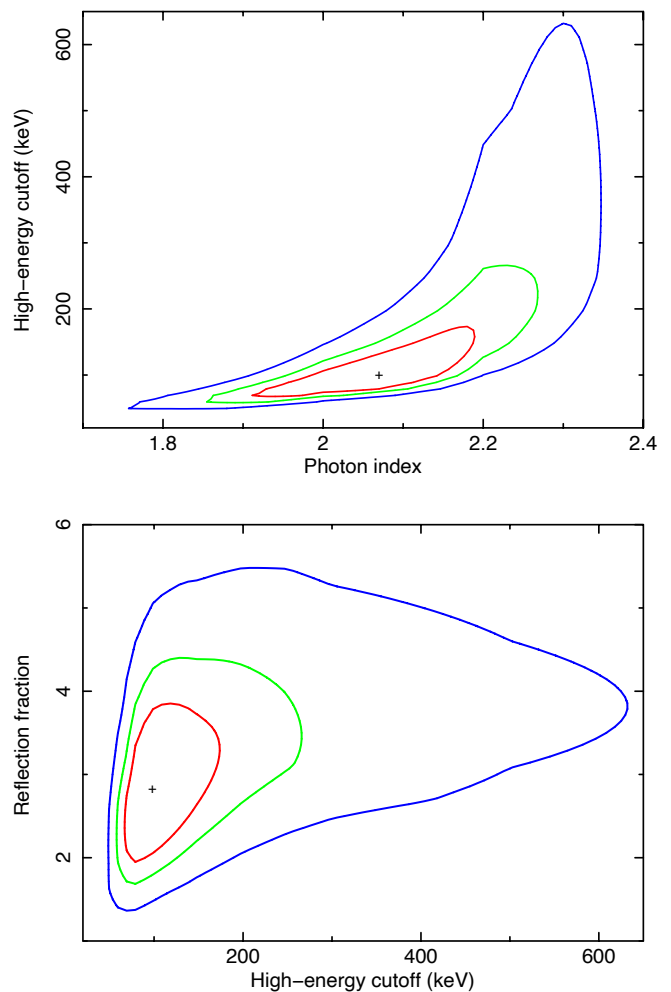


Fig. 2: Confidence contours of reflection parameters obtained with an *axill* model (see Sect. 3.1 and Table 2). *Top*: High-energy cutoff vs. photon index. *Bottom*: Reflection fraction vs. high-energy cutoff. Contours are color-coded as follows: red, green, blue for 68%, 90%, 99% confidence level, respectively.

data including *zgauss* components where the blind search and the residuals to model *axill* (Fig. 1, panel (e)) showed hints of absorption lines.

XMM 301 presents no signs of emission or absorption features additional to those already included in *xillver*, while XMM 101 shows hints of a narrow absorption line at $E_{rest} = 11.7 \pm 0.2$ keV ($\Delta Cstat/\Delta\nu = 9/2$, rest-frame width set to 0.1 keV). We ran Monte Carlo simulations (Protassov et al. 2002) to measure the real significance of the 11 keV line, by simulating 10^4 broadband spectra from our *axill* best fit model (see Table 2) using the *fakeit* function of *Xspec*. By searching the simulated spectra for the detection of spurious emission and absorption lines, we built the posterior probability distribution of finding a real detection. Applying such a distribution to the line at 11.7 keV in XMM 101, we find that its significance is lower than the 90% confidence level. Thus, we find that no UFO features are present in the latest X-ray data of APM 08279.

Table 2: Summary of the best-fit parameters of each model tested on 2019 data.

Model (1)	Γ (2)	N_{H} (3)	E_{cut} (4)	$E_{\text{Fe K}\alpha}$ (5)	$EW_{\text{Fe K}\alpha}$ (6)	R (7)	$Cstat (\nu)$ (8)
pl	1.35 ± 0.03	–	–	–	–	–	3312 (3080)
acutpl	1.3 ± 0.1	4.7 ± 0.8	36_{-7}^{+10}	–	–	–	2812 (3078)
acutpl+K α	1.2 ± 0.1	3.9 ± 0.8	33_{-6}^{+8}	6.5 ± 0.1	318_{-90}^{+94}	–	2775 (3076)
axill	$2.1_{-0.2}^{+0.1}$	6.4 ± 0.8	99_{-35}^{+91}	–	–	$2.8_{-0.9}^{+1.1}$	2728 (3077)

Notes. Column 1: Model name; Col. 2: Photon index; Col. 3: Column density in excess of the Galactic value (units of 10^{22} cm^{-2}); Col. 4: High-energy cutoff rest-frame energy (keV); Cols. 5-6: Rest-frame energy (keV) and equivalent width (eV) of Fe K α emission line; Col. 7: Reflection fraction; Col. 8: $Cstat$ (degrees of freedom ν). The line width of the Fe K α is set to $\sigma = 0.1$ keV rest frame. All errors are computed at the 90% confidence level for one parameter of interest. *Model list:* Model pl = phabs*zphabs*zpo; Model acutpl = phabs*zphabs*zcutoffpl; Model acutpl+K α = phabs*zphabs*(zcutoffpl+zgauss); Model arefl+K α = phabs*zphabs*(pextrav+zgauss); Model axill = phabs*zphabs*xillver. All models include Galactic absorption ($N_{\text{H}} = 4.2 \times 10^{20} \text{ cm}^{-2}$).

4. X-ray reflection in previous observations

During 2019 exposures, APM 08279 turned out to be fainter than what was previously expected (see Fig. 3, upper panel, and Tables 1 and 3), and clearly showed X-ray reflection signatures for the first time. We thus collected all previous XMM-Newton and Chandra X-ray observations with the aim of answering the following questions: namely, whether X-ray reflection was already in place before 2019 and, thus, how that would relate to what was observed in 2019.

By referring to literature studies (H02; C09), we left out of the data sample the first Chandra exposure, the shortest one, because of the low count statistics. Table 3 summarizes the relevant information about archival observations, including the acronyms that we use to indicate them. We refer to H02 for the analysis of XMM1 and to C09 for the remaining five (CXO2, XMM2, XMM3, XMM4, CXO3). We reduced the selected Chandra (CXO2, CXO3) and XMM-Newton (XMM1, XMM2, XMM3, XMM4) archival exposures to uniformly apply the latest calibration files, filtering high-background intervals in XMM-Newton data using the same GTI thresholds of C09. The count statistics of these spectra is much higher than that of 2019 data, thanks to the higher flux of APM 08279 and to the longer exposures. Similarly to the approach of C09, spectra with more than 10^4 cts were grouped to 100 cts/bin (EPIC-pn data of XMM2, XMM3, XMM4), while those with few 10^3 cts to 20 cts/bin (XMM1 EPIC-pn, all EPIC-MOS and Chandra spectra). We thus applied χ^2 statistics in the spectral analysis of past observations, jointly fitting EPIC-pn and -MOS spectra collected in the same epoch.

To probe the X-ray reflection, we first drew on the best-fit models from the literature. H02 fit XMM1 data with an absorption edge, whereas C09 fit the spectra firstly using phenomenological models, where the UFOs are modeled only through their main absorption imprint, and secondly using Xstar analytical models (warmabs). Testing X-ray reflection while already accounting for UFOs through warmabs is a non-trivial exercise, so we selected the phenomenological representation of past data (Model 6, C09). We then tested the X-ray reflection by replacing the single power-law emission of literature phenomenological best-fit models with a xillver component (lit_xill model). We set the absorption-edge parameters in XMM1 to those reported by H02. Both energy and width of the UFO absorption lines are set to those presented in C09 and we leave their normalization free to vary. The lack of high-energy coverage in past observations prevents us from constraining the high-energy cutoff. We thus set it to the value measured in 2019 data ($E_{\text{cut}} = 100$ keV), safely far from the high-energy end of Chandra and XMM-

Newton spectra. We also set the reflection inclination angle to $i = 30^\circ$, as done in Sect. 3.1, and assume a low-ionization reflecting medium as found for 2019 data ($\log(\xi/\text{erg s}^{-1} \text{ cm}) = 1.7$).

We investigated the evolution of the source emission through the epochs using three probes: *i*) the 2–10 keV observed-band total source flux, *ii*) the 2–10 keV observed-band flux of the reflection component only, and *iii*) the reflection fraction R . To measure probe *ii*), we built a pure-reflection model using xillver with $R = -1$, setting its normalization to the best-fit value of the respective lit_xill model scaled by the measured reflection fraction. When R is only constrained as an upper limit, we derived an upper limit to the 2–10 keV observed-band reflection flux. When R is constrained (as is for XMM3 and 2019 data), we measured the reflection flux by scaling the normalization of the lit_xill model by the best fit value of R . We then assigned as uncertainty the spread in flux obtained by scaling the normalization by the respective upper and lower 90% confidence level values of R . Figure 3 shows the evolution of the three probes across the considered observing epochs. The source X-ray flux (upper panel) presents a factor of 1.5 decrease between the period 2000–2008 and 2019 while, despite the many upper limits, the reflection flux (middle panel) is fully consistent with showing no trend across the years. The 2–10 keV observed-energy band corresponds to $\approx 9.8 - 49$ keV in the $z = 3.91$ rest-frame, which is where X-ray reflection induces the so-called “reflection hump” and where flux suppression by absorption is strong only in Compton-thick AGN (e.g., Maiolino et al. 1998; Bassani et al. 1999; Matt et al. 2000). Regarding the obscuration hypothesis, we find no evolution in the column density of the low-ionization absorber; the one measured in 2019 data (see Sect. 3.1 and Table 2) is consistent with results from the literature (H02; C09). As a consequence, the reduction in flux must be ascribed to a decrease of the source primary activity. The trend (or lack of it) in the first two panels of Fig. 3 is indeed well matched by the evolution of R (lower panel) which, despite the large uncertainties, shows a discontinuity between 2019 and epochs prior to 2008. Coupling the three probes together suggests that the reflection component seen in 2019 data was likely already in place before 2008, but less evident due to a stronger primary continuum.

In this scenario, the reflection component observed in 2019 can possibly be interpreted as the echo of APM 08279 previous activity, due to *i*) the time delay between the X-ray source and the reflector and *ii*) the reduced direct emission observed in the last epoch. This is similar to the case of PG 1247+267: Lanzuisi et al. (2016) explain its very high reflection fraction in terms of X-ray source variability, namely, the primary emission has dropped but the reflection still has not due to the additional

Table 3: Log of APM 08279+5255 past observations and reflection parameters

Name	ObsID	Date	MJD	Total Exp.	f_{2-10}	Ref.	R
CXO1	1643	2000 Oct 11	51828	9.1	$5.5^{+0.3}_{-0.5}$	a	–
XMM1	0092800101	2001 Oct 30	52212	16.5	$4.3^{+0.1}_{-0.2}$	a	< 1.1
CXO2	2979	2002 Feb 24	52329	88.8	$4.3^{+0.1}_{-0.1}$	b	< 0.7
XMM2	0092800201	2002 Apr 28	52392	102.3	$4.1^{+0.1}_{-0.1}$	a, b	< 1.4
XMM3	0502220201	2007 Oct 06	54379	89.6	$3.9^{+0.1}_{-0.1}$	b	$1.2^{+0.3}_{-0.3}$
XMM4	0502220301	2007 Oct 22	54395	90.5	$5.0^{+0.1}_{-0.1}$	b	< 1.1
CXO3	7684	2008 Jan 14	54479	88.1	$4.5^{+0.2}_{-0.2}$	b	< 0.9

Notes. Absorbed fluxes are estimated in the 2–10 keV observed-band from phenomenological models, and are given in units of 10^{-13} erg cm $^{-2}$ s $^{-1}$, with errors given at 68% confidence level. The absorbed flux of CXO1 and XMM1 is evaluated from reanalyzed data (see Sect. 4), while the other values are taken from the literature (references: a. H02, b. C09). The total exposure is given in units of ks. The reflection fraction is obtained using lit_xill model), i.e. a zphabs*zedge*xillver model for XMM1 and a zphabs*(xillver+zgauss+zgauss) model for the other data. Values for the absorber, the edge and the absorption lines are set to the best fit of H02 and C09. Errors and upper limits on the reflection fraction are given at the 90% confidence level.

light-travel path. Using the same argument, we can place a lower limit on the distance between reflector and X-ray corona, assuming that the variability during the 2008–2019 observational gap is only ascribed to a uniform decrease in the activity of the X-ray corona. We consider the time elapsed between CXO3 and XMM 101 ($\Delta t = 832.4$ d in the quasar rest frame) as that corresponding to the light travel path between X-ray source and reflector ($r_{\text{refl}} = c\Delta t$). Under this assumption, we derive the lower limit to the reflector location as $r_{\text{refl}} \gtrsim 0.7$ pc (in accordance to the lower limit obtained from the Fe K α line width: $r_{\text{Fe K}\alpha} \gtrsim 0.04$ pc), which definitely excludes a disc origin in favor of a distant reflector. By this lower limit, the reflection likely happens in the molecular torus (e.g., Burtscher et al. 2013; Netzer 2015) or, based on the estimate by Saturni et al. (2016) for this quasar, at the boundary of the broad-line region.

5. Properties of the X-ray corona

We presented a detailed analysis of the first *NuSTAR* observations of APM 08279, a gravitationally lensed, broad-absorption line quasar at $z = 3.91$, taken jointly to the latest XMM-*Newton* exposures in 2019. By means of primary-emission decrease (see Sect. 4) and high-energy sampling, we are able for the first time to see and constrain a strong reflection component ($R = 2.8^{+1.1}_{-0.9}$) and the high-energy cutoff ($E_{\text{cut}} = 99^{+91}_{-35}$ keV) in this source. Despite the large uncertainties, the high-energy cutoff of APM 08279 is fully consistent with the only other estimates at $z > 1$ (Dadina et al. 2016; L19; see also the tentative measure of Lanzuisi et al. 2016). We thus break the previous redshift record of B1422 (Dadina et al. 2016; L19) and find additional evidence for complex emission mechanisms, very much alike those of local Seyfert galaxies, in high- z AGN (up to $z \approx 4$). It is of interest to notice that we do not find evidence for significant X-ray winds in the 2019 observations of APM 08279, the archetype of high- z UFOs. While these winds are known to be variable and episodic events (e.g., Dadina et al. 2005; Cappi et al. 2006; Giustini et al. 2011; Gofford et al. 2014; Igo et al. 2020; Parker et al. 2021), the present data do not allow us to investigate further on their disappearance. Only a new, dedicated monitoring will be key in probing *i*) whether this new flux state is enduring, *ii*) whether UFOs are no longer a distinctive feature of APM 08279, and *iii*) whether the former might be the cause of the latter.

The measured reflection fraction ($R = 2.8^{+1.1}_{-0.9}$) is, even considering the large uncertainties, much higher than what expected based on previous results in the literature for high-luminosity sources: AGN with $L_X > 10^{45}$ erg s $^{-1}$ are usually found to show $R < 1$ (Del Moro et al. 2017; Zappacosta et al. 2018). We note that even though lower than our estimate, both the reflection fractions measured in L19 are higher than what expected for high-luminosity sources. However, the case of APM 08279 during 2019 exposures quite differs from those of B1422 and 2MASSJ16, and is more alike that of PG 1247+267, as discussed in Sect. 4. Moreover, the Fe K α EW of APM 08279, measured with the phenomenological model acutpl+K α (Table 2), is larger than the expectation based on the results over samples of high- z and local AGN (e.g., Falocco et al. 2013) and on the Iwasawa-Taniguchi effect (Bianchi et al. 2007), but is consistent, at 90% confidence level, with the highest EWs of the CAIXA sample (corresponding to the 98% percentile of the EW distribution, Bianchi et al. 2009). In fact, such high values of R and of Fe K α EW in 2019 data, coupled with the non-evolution of the X-ray reflection flux in the 2–10 keV observed band and the lower limit placed on the reflector’s distance, likely hint that the reflection component in this last observation could be the echo of APM 08279 previous activity. Moreover, the majority of the reflection fraction values obtained from data prior to 2008 (see Fig. 3 and Table 3) are in decent agreement with what expected from the literature ($R < 1$). This is additional proof for our interpretation of APM 08279 activity variation (see Sect. 4), and for the Seyfert-like mechanisms that give origin to its emission.

L19 adopted the $\ell - \theta$ plane of Fabian et al. (2015) translated into the directly observable quantities L_X versus E_{cut} , respectively, through Eqs. (1) (with $K = 2$, as assumed in Fabian et al. 2015) and (2). In the same way, theoretical $\ell(\theta)$ critical lines of Stern et al. (1995) were converted into $L_X(E_{\text{cut}})$ thresholds, assuming a corona size $R_X = 5 r_S$ (Schwarzschild radius: $r_S = 2GM_{\text{BH}}/c^2$) and SMBH masses $M_{\text{BH}} = 10^8 M_\odot$ and $10^9 M_\odot$, namely, representative of the sample of Fabian et al. (2015) and of powerful, high- z quasars, respectively. L19 also updated the compilation by Fabian et al. (2015) with more recent E_{cut} measurements, obtained both with and without *NuSTAR* data, and both on individual targets or over samples of sources (e.g., Malizia et al. 2014; Tortosa et al. 2017; Buisson et al. 2018; Molina et al. 2019). L19 included also the median values, binned in compactness (i.e., L_X), of the large BASS sample of local AGN as measured by Ricci et al. (2018). Figure 4 (left) shows

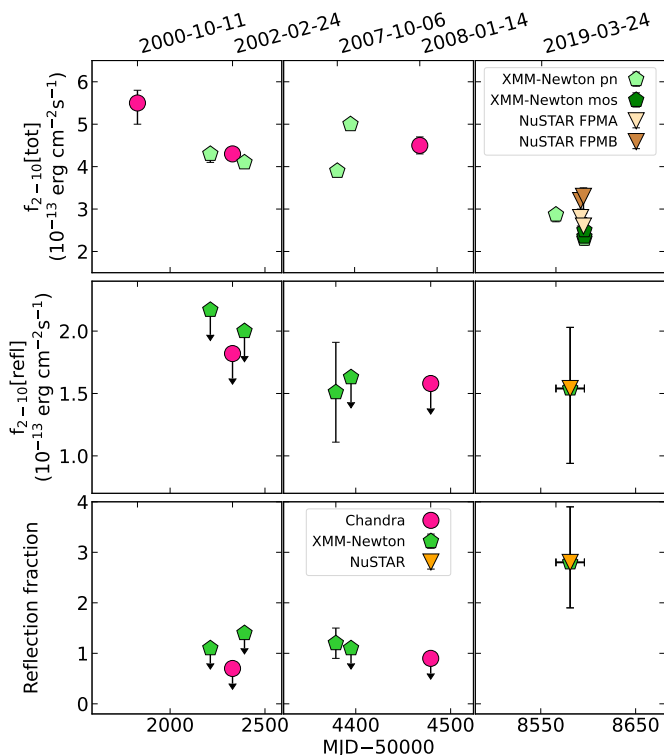


Fig. 3: Variation of 2–10 keV observed-band total source flux (top panel), 2–10 keV observed-band flux of the reflection component alone (middle panel) and reflection fraction R (bottom panel), of *Chandra* (magenta circles), *XMM-Newton* (light, dark and medium green pentagons for EPIC pn, EPIC MOS, and EPIC pn+MOS, respectively) and *NuSTAR* (ivory, brown, and orange triangles for FPMA, FPMB, and FPMA+FPMB, respectively) data from year 2000 to 2019. Top axis shows the dates, bottom axis the modified Julian dates. *Top panel*: Values up to 2009 are taken from C09, the first two points are evaluated from re-analyzed data. Errors are given at 68% confidence, as in C09. When they are not visible, errorbars are smaller than the point size. *Middle panel*: Upper limits are computed using the 90% upper limit of the reflection fraction. *Bottom panel*: Upper limits are computed at 90% confidence level. The first *Chandra* observation (i.e., the shortest one – see main text) is left out due to the low count statistics.

the $L_X - E_{\text{cut}}$ plane of L19 further updated with our measurement, the pair-production critical lines for $M_{\text{BH}} = 10^{10} M_{\odot}$, and results from other recent works, derived through canonical modeling of the continuum (Kara et al. 2017; Tortosa et al. 2018; Kamraj et al. 2018; Ursini et al. 2020; Baloković et al. 2020; Middei et al. 2020, 2021; Reeves et al. 2021, see also Ezhikode et al. 2020, where the authors model X-ray reflection accounting for relativistic effects). When multiple estimates for a same source are available, we only kept the latest one. We also added earlier measurements of Dadina (2007) that were not revised in later works, and selecting the best constrained value in case of multiple measurements for a single source. Akylas & Georgantopoulos (2021) recently studied the distribution of coronal temperatures in a big sample of Seyfert 1 selected by *Swift* and followed up by *NuSTAR* (118 sources, many also comprised in Ricci et al. 2017, 2018). Figure 4 shows the median high-energy cutoff of Seyfert

1 galaxies measured by Akylas & Georgantopoulos (2021). Recent works by Saturni et al. (2016, 2018) have agreed on APM 08279 data being best reproduced by low magnification factors ($\mu_L \lesssim 9$). To add our target to the $L_X - E_{\text{cut}}$ plane, we estimated the de-absorbed and de-lensed 2–10 keV luminosity of APM 08279 ($L_X = 6.5 \times 10^{45} \text{ erg s}^{-1}$) assuming a magnification factor of $\mu_L = 4$ (Riechers et al. 2009). Like the other high- z AGN, APM 08279 falls in the allowed region for high-mass SMBHs with X-ray luminosity higher than $2 \times 10^{45} \text{ erg s}^{-1}$. Being located in the proximity of the central SMBH, hot coronae are subject to the laws of general relativity (e.g., Wilkins et al. 2021). Tamborra et al. (2018) provide correction factors to be applied to results obtained through canonical reflection models. The authors demonstrate that, without accounting for general relativity, the observed high-energy cutoff (E_{cut}^o) underestimates the intrinsic value E_{cut}^i by a factor $g = E_{\text{cut}}^i / E_{\text{cut}}^o$. Tamborra et al. (2018) compute g -factors for a variety of combinations of corona properties and reflection inclination angles. Assuming a $5 r_S$ corona and an inclination angle $i = 30^\circ$ (see Sect. 3.1), the corresponding g -factor spans between 1.2 and 1.5. Even assuming the maximum value, the 90% confidence level upper bound of the high-energy cutoff of APM 08279 falls below the critical line for a slab corona and $M_{\text{BH}} = 10^{10} M_{\odot}$. Thus, APM 08279 would still lie in the allowed region of the $L_X - E_{\text{cut}}$ plane for a SMBH mass of $\approx 10^{10} M_{\odot}$ even when general relativity effects are accounted for.

L19 found that the median cutoff energy expected for local BASS AGN (Ricci et al. 2018) in the same accretion regime as their high- z sources was much higher than the measured values of B1422 and 2MASSJ16. For what concerns APM 08279, local AGN in the same Eddington regime as our target ($\lambda_{\text{Edd}} \approx 0.4$, Saturni et al. 2018) show a median high-energy cutoff of $E_{\text{cut}} \approx 170 \text{ keV}$, which is well above the best-fit measurement ($E_{\text{cut}} \approx 99 \text{ keV}$) but consistent with its 90% confidence range ($68 \text{ keV} < E_{\text{cut}} < 190 \text{ keV}$). However, the existence of a relation between high-energy cutoff and Eddington ratio was recently debated in the literature: Hinkle & Mushotzky (2021) and Kamraj et al. (2022) find no correlation between accretion parameters and the high-energy cutoff in their new analyses of BASS AGN, as opposed to what seen by Ricci et al. (2018). According to their spectral analysis of *NuSTAR* data alone of *Swift*/BAT selected AGN, Kang & Wang (2022) confirmed the absence of a $E_{\text{cut}} - \lambda_{\text{Edd}}$ relation and, interestingly, they find that some sources fall in the runaway pair-production region of Fig. 4. Only a better sampling of both the high-luminosity end and the high-accretion regime will allow us to better understand the physics regulating hot coronae in powerful AGN. Lastly, we addressed the possibility of APM 08279 having a magnification factor more similar to $\mu_L = 100$ (Egami et al. 2000), which would make our target a more "regular" AGN ($L_X(\mu_L = 100) = 2.6 \times 10^{44} \text{ erg s}^{-1}$, $\lambda_{\text{Edd}}(\mu_L = 100) \approx 0.08$). Nevertheless, APM 08279 would still fall in the allowed region of the $L_X - E_{\text{cut}}$ plane and its high-energy cutoff would not be consistent with the median value of BASS AGN in a similar accretion regime.

6. Summary and conclusions

We presented our analysis of the first X-ray broadband spectrum of APM 08279, a gravitationally lensed, broad-absorption line quasar at $z = 3.91$. We then compared our findings with past observations and we summarize our key results here:

- We measured a long-lasting X-ray reflection component in this source for the first time. We find it consistent with being

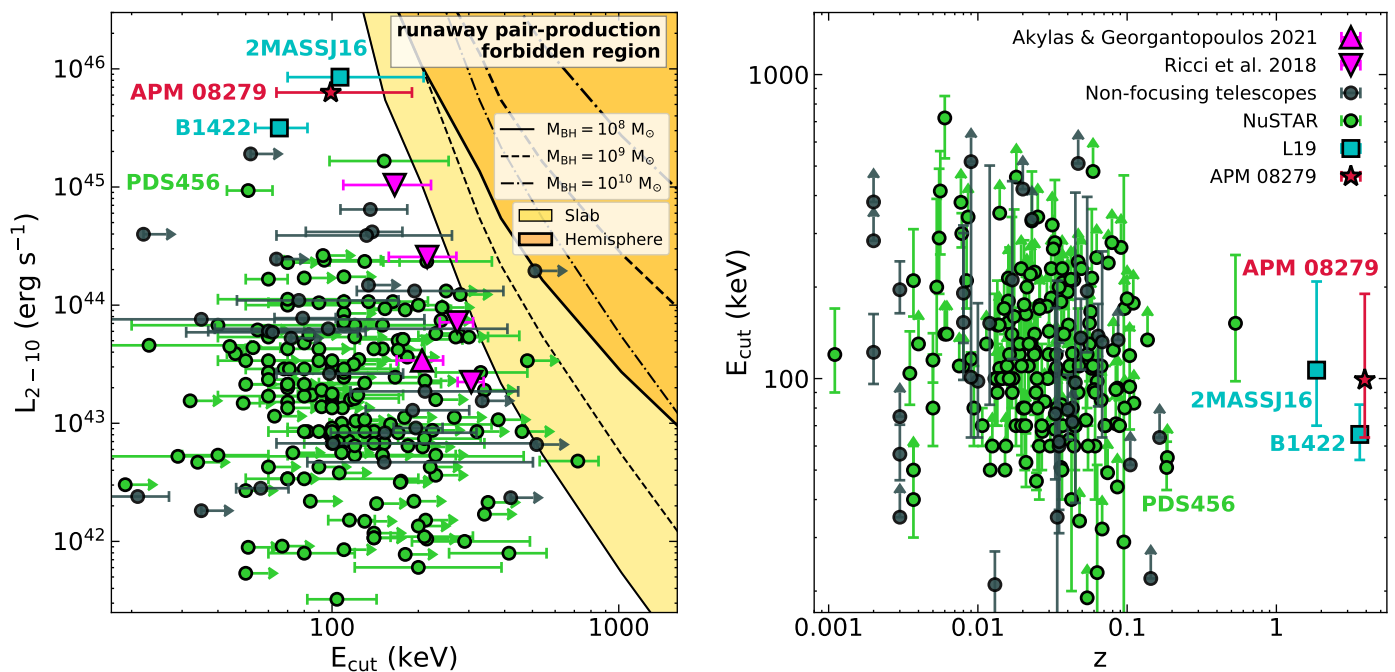


Fig. 4: Compactness–temperature diagram translated into directly observable quantities and high-energy cutoff distribution as a function of redshift. *Left*: X-ray luminosity vs. high-energy cutoff, updated from L19 (see main text and Tables A.1–A.3 for details). *NuSTAR* measurements are in green, non-focusing telescopes’ in grey, high- z AGN from L19 in cyan, and our measurement in red. Magenta downward triangles mark the averaged values for BASS AGN from Ricci et al. (2018), while the magenta upward triangle marks the median point of Seyfert 1 galaxies from Akylas & Georgantopoulos (2021). Yellow (orange) areas delimited by a thin (thick) line show the runaway pair-production region for a $10^8 M_{\odot}$ SMBH in the case of slab (hemisphere) geometry. Dashed (dashed-dotted) lines mark the same thresholds for a $10^9 M_{\odot}$ ($10^{10} M_{\odot}$) SMBH. *Right*: High-energy cutoff vs. redshift plane for the same samples as in the left panel.

produced by distant material, in the molecular torus or at the boundary of the broad-line region ($r_{\text{refl}} \gtrsim 0.7$ pc). The large reflection fraction of $R \simeq 2.8^{+1.1}_{-0.9}$ is interpreted in terms of a decrease in the primary X-ray emission, as, for instance, the case of PG 1247+267.

- We break the previous redshift record for the farthest high-energy cutoff ever observed. Our measurement of $E_{\text{cut}} = 99^{+91}_{-35}$ keV is fully in agreement with previous results on high- z , high-luminosity AGN.
- As opposed to the other high- z sources of L19, the cutoff measured for APM 08279 is consistent (within a 90% confidence level) with the median values of BASS AGN in the same accretion regime. A better sampling of this luminosity regime will be key to study the behavior of such sources.

Results that have come about over the last two decades have shown that studies of high- z AGN are observationally challenging but highly rewarding, when carried out by means of long-enough exposures of present-day observatories. Next-generation X-ray telescopes will be crucial in substantially expanding the samples used to test the physical processes that regulate hot coronae. In particular, enlarging the sample of high- z AGN, especially at the fainter end, will shed light on whether low- and high- z AGN comply with the same relations. Would they differ, only future studies of high- z AGN will disclose whether it is owed to the different luminosity regimes or whether it is a byproduct of a potential evolution with cosmic time. To this aim, the *eROSITA* All-Sky Survey will be key in discovering new high- z AGN, to then be followed up by present facilities such as *NuSTAR* and, hopefully, future hard X-ray instruments.

Acknowledgements. We acknowledge financial support from ASI under grants ASI-INAF I/037/12/0 and n. 2017-14-H.O., and from the grant PRIN MIUR 2017PH3WAT (‘Black hole winds and the baryon life cycle of galaxies’). This work is based on observations obtained with *XMM-Newton*, an ESA science mission with instruments and contributions directly funded by ESA Member States and the USA (NASA). This research has made use of data obtained from the *Chandra* Data Archive, and software provided by the *Chandra* X-ray Center (CXC) in the application package CIAO. This research has made use of data and/or software provided by the High Energy Astrophysics Science Archive Research Center (HEASARC), which is a service of the Astrophysics Science Division at NASA/GSFC. This work made use of data from the *NuSTAR* mission, a project led by the California Institute of Technology, managed by the Jet Propulsion Laboratory, and funded by the NASA. This research has made use of the *NuSTAR* Data Analysis Software (*NuSTAR*DAS) jointly developed by the ASI Science Data Center (ASDC, Italy) and the California Institute of Technology (USA).

References

- Akylas, A. & Georgantopoulos, I. 2021, *A&A*, 655, A60
Baloković, M., Harrison, F. A., Madejski, G., et al. 2020, *ApJ*, 905, 41
Bassani, L., Dadina, M., Maiolino, R., et al. 1999, *The Astrophysical Journal Supplement Series*, 121, 473
Bianchi, S., Guainazzi, M., Matt, G., & Fonseca Bonilla, N. 2007, *A&A*, 467, L19
Bianchi, S., Guainazzi, M., Matt, G., Fonseca Bonilla, N., & Ponti, G. 2009, *A&A*, 495, 421
Buisson, D. J. K., Parker, M. L., Kara, E., et al. 2018, *MNRAS*, 480, 3689
Burtscher, L., Meisenheimer, K., Tristram, K. R. W., et al. 2013, *A&A*, 558, A149
Cappi, M., Panessa, F., Bassani, L., et al. 2006, *A&A*, 446, 459
Cappi, M., Tombesi, F., Bianchi, S., et al. 2009, *A&A*, 504, 401
Cash, W. 1979, *ApJ*, 228, 939
Cavaliere, A. & Morrison, P. 1980, *ApJ*, 238, L63
Chartas, G., Agol, E., Eracleous, M., et al. 2002, *ApJ*, 568, 509

- Chartas, G., Saez, C., Brandt, W. N., Giustini, M., & Garmire, G. P. 2009, *ApJ*, 706, 644
- Costa, T., Pakmor, R., & Springel, V. 2020, *MNRAS*, 497, 5229
- Dadina, M. 2007, *A&A*, 461, L209
- Dadina, M. 2008, *A&A*, 485, 417
- Dadina, M., Cappi, M., Malaguti, G., Ponti, G., & de Rosa, A. 2005, *A&A*, 442, 461
- Dadina, M., Vignali, C., Cappi, M., et al. 2016, *A&A*, 592, A104
- Dauser, T., Garcia, J., Parker, M. L., Fabian, A. C., & Wilms, J. 2014, *MNRAS*, 444, L100
- de Rosa, A., Panessa, F., Bassani, L., et al. 2012, *MNRAS*, 420, 2087
- Del Moro, A., Alexander, D. M., Aird, J. A., et al. 2017, *ApJ*, 849, 57
- Egami, E., Neugebauer, G., Soifer, B. T., et al. 2000, *ApJ*, 535, 561
- Ellison, S. L., Ibat, R., Pettini, M., et al. 2004, *A&A*, 414, 79
- Ezhikode, S. H., Dewangan, G. C., Misra, R., & Philip, N. S. 2020, *MNRAS*, 495, 3373
- Fabian, A. C., Lohfink, A., Kara, E., et al. 2015, *MNRAS*, 451, 4375
- Falocco, S., Carrera, F. J., Corral, A., et al. 2013, *A&A*, 555, A79
- Faucher-Giguère, C.-A. & Quataert, E. 2012, *MNRAS*, 425, 605
- Gandhi, P., Fabian, A. C., Suebsuwong, T., et al. 2007, *MNRAS*, 382, 1005
- García, J., Dauser, T., Lohfink, A., et al. 2014, *ApJ*, 782, 76
- Giustini, M., Cappi, M., Chartas, G., et al. 2011, *A&A*, 536, A49
- Gofford, J., Reeves, J. N., Braitto, V., et al. 2014, *ApJ*, 784, 77
- Guilbert, P. W., Fabian, A. C., & Rees, M. J. 1983, *MNRAS*, 205, 593
- Haardt, F. & Maraschi, L. 1991, *ApJ*, 380, L51
- Haardt, F., Maraschi, L., & Ghisellini, G. 1994, *ApJ*, 432, L95
- Harrison, F. A., Craig, W. W., Christensen, F. E., et al. 2013, *ApJ*, 770, 103
- Hasinger, G., Schartel, N., & Komossa, S. 2002, *ApJ*, 573, L77
- HI4PI Collaboration, Ben Bekhti, N., Flöer, L., et al. 2016, *A&A*, 594, A116
- Hinkle, J. T. & Mushotzky, R. 2021, *MNRAS*, 506, 4960
- Igo, Z., Parker, M. L., Matzeu, G. A., et al. 2020, *MNRAS*, 493, 1088
- Irwin, M. J., Webster, R. L., Hewett, P. C., Corrigan, R. T., & Jędrzejewski, R. I. 1989, *AJ*, 98, 1989
- Just, D. W., Brandt, W. N., Shemmer, O., et al. 2007, *ApJ*, 665, 1004
- Kammoun, E. S., Risaliti, G., Stern, D., et al. 2017, *MNRAS*, 465, 1665
- Kamraj, N., Brightman, M., Harrison, F. A., et al. 2022, *ApJ*, 927, 42
- Kamraj, N., Harrison, F. A., Baloković, M., Lohfink, A., & Brightman, M. 2018, *ApJ*, 866, 124
- Kang, J.-L. & Wang, J.-X. 2022, arXiv e-prints, arXiv:2203.07118
- Kara, E., García, J. A., Lohfink, A., et al. 2017, *MNRAS*, 468, 3489
- King, A. & Pounds, K. 2015, *ARA&A*, 53, 115
- Koss, M., Trakhtenbrot, B., Ricci, C., et al. 2017, *ApJ*, 850, 74
- Lanzuisi, G., Gilli, R., Cappi, M., et al. 2019, *ApJ*, 875, L20
- Lanzuisi, G., Perna, M., Comastri, A., et al. 2016, *A&A*, 590, A77
- Leung, T. K. D., Hayward, C. C., Casey, C. M., et al. 2019, *ApJ*, 876, 48
- Maiolino, R., Salvati, M., Bassani, L., et al. 1998, *A&A*, 338, 781
- Malizia, A., Molina, M., Bassani, L., et al. 2014, *ApJ*, 782, L25
- Matt, G., Fabian, A. C., Guainazzi, M., et al. 2000, *MNRAS*, 318, 173
- Middei, R., Matzeu, G. A., Bianchi, S., et al. 2021, *A&A*, 647, A102
- Middei, R., Tombesi, F., Vagnetti, F., et al. 2020, *A&A*, 635, A18
- Miniutti, G. & Fabian, A. C. 2006, *MNRAS*, 366, 115
- Molina, M., Bassani, L., Malizia, A., et al. 2013, *MNRAS*, 433, 1687
- Molina, M., Bassani, L., Malizia, A., et al. 2009, *MNRAS*, 399, 1293
- Molina, M., Malizia, A., Bassani, L., et al. 2019, *MNRAS*, 484, 2735
- Netzer, H. 2015, *ARA&A*, 53, 365
- Parker, M. L., Alston, W. N., Härer, L., et al. 2021, *MNRAS*, 508, 1798
- Petrucchi, P. O., Haardt, F., Maraschi, L., et al. 2001, *ApJ*, 556, 716
- Piconcelli, E., Jimenez-Bailón, E., Guainazzi, M., et al. 2005, *A&A*, 432, 15
- Planck Collaboration, Aghanim, N., Akrami, Y., et al. 2020, *A&A*, 641, A6
- Protassov, R., van Dyk, D. A., Connors, A., Kashyap, V. L., & Siemiginowska, A. 2002, *ApJ*, 571, 545
- Reeves, J. N., Braitto, V., Porquet, D., et al. 2021, *MNRAS*, 500, 1974
- Ricci, C., Ho, L. C., Fabian, A. C., et al. 2018, *MNRAS*, 480, 1819
- Ricci, C., Trakhtenbrot, B., Koss, M. J., et al. 2017, *ApJS*, 233, 17
- Riechers, D. A., Walter, F., Carilli, C. L., & Lewis, G. F. 2009, *ApJ*, 690, 463
- Saez, C., Chartas, G., & Brandt, W. N. 2009, *ApJ*, 697, 194
- Saturni, F. G., Bischetti, M., Piconcelli, E., et al. 2018, *A&A*, 617, A118
- Saturni, F. G., Trevese, D., Vagnetti, F., Perna, M., & Dadina, M. 2016, *A&A*, 587, A43
- Stacey, H. R., McKean, J. P., Robertson, N. C., et al. 2018, *MNRAS*, 476, 5075
- Stern, B. E., Poutanen, J., Svensson, R., Sikora, M., & Begelman, M. C. 1995, *ApJ*, 449, L13
- Tamborra, F., Papadakis, I., Dovčiak, M., & Svoboda, J. 2018, *MNRAS*, 475, 2045
- Tortosa, A., Bianchi, S., Marinucci, A., Matt, G., & Petrucci, P. O. 2018, *A&A*, 614, A37
- Tortosa, A., Marinucci, A., Matt, G., et al. 2017, *MNRAS*, 466, 4193
- Ursini, F., Petrucci, P. O., Bianchi, S., et al. 2020, *A&A*, 634, A92
- Vasudevan, R. V., Brandt, W. N., Mushotzky, R. F., et al. 2013, *ApJ*, 763, 111
- Vignali, C., Brandt, W. N., Schneider, D. P., & Kaspi, S. 2005, *AJ*, 129, 2519
- Vignali, C., Comastri, A., Cappi, M., et al. 1999, *ApJ*, 516, 582
- Wilkins, D. R., Gallo, L. C., Costantini, E., Brandt, W. N., & Blandford, R. D. 2021, *Nature*, 595, 657
- Younes, G., Ptak, A., Ho, L. C., et al. 2019, *ApJ*, 870, 73
- Zappacosta, L., Comastri, A., Civano, F., et al. 2018, *ApJ*, 854, 33

Appendix A: High-energy cutoff measurements by *NuSTAR* and nonfocusing telescopesTable A.1: Literature low- z measurements collected by L19

Source	z	$\log L_{2-10}$	E_{cut}	Flag	References
NGC 5506	0.006	42.68	720^{+130}_{-190}	1	(a),(b)
NGC 7213	0.006	42.07	< 140	1	(a),(b)
MCG-6-30-15	0.008	43.39	< 110	1	(a),(b)
MCG 5-23-16	0.009	43.2	116^{+6}_{-5}	1	(a),(b)
SWIFT J2127.4+5654	0.014	43.0	108^{+11}_{-10}	1	(a),(b)
NGC 5548	0.018	43.3	70^{+40}_{-10}	1	(a),(b)
Mrk 335	0.026	42.51	< 174	1	(a),(b)
1H0707-495	0.041	43.06	< 63	1	(a),(b)
Fairall 9	0.047	43.98	< 242	1	(a),(b)
Cyg A	0.056	44.24	< 110	1	(a),(b)
3C 382	0.058	44.37	214^{+147}_{-63}	1	(a),(b)
IGR J0033+6122	0.105	45.28	< 52	2	(c),(a),(b)
3C 111	0.049	44.81	136^{+47}_{-29}	2	(c),(a),(b)
IGR J07597-3842	0.04	43.89	79^{+24}_{-16}	2	(c),(a),(b)
NGC 3783	0.01	43.42	98^{+79}_{-34}	2	(c),(a),(b)
NGC 4151	0.003	42.96	196^{+47}_{-32}	2	(c),(a),(b)
IGR J16558-5203	0.054	44.12	194^{+202}_{-72}	2	(c),(a),(b)
1H2251-179	0.064	44.62	138^{+38}_{-57}	2	(c),(a),(b)
MCG-02-58-022	0.047	44.29	< 510	2	(c),(a),(b)
MCG+08-11-011	0.021	44.03	163^{+53}_{-32}	1	(d),(b)
Mrk 6	0.019	43.21	120^{+51}_{-28}	1	(d),(b)
IGR J12415-5750	0.024	43.24	123^{+54}_{-47}	1	(d),(b)
IC4329A	0.016	43.97	153^{+20}_{-16}	1	(d),(b)
GRS 1734-292	0.021	43.64	53^{+13}_{-9}	1	(d),(b)
3C 390.3	0.056	44.37	130^{+42}_{-32}	1	(d),(b)
NGC 6814	0.005	42.18	115^{+26}_{-18}	1	(d),(b)
4C 74.24	0.104	44.38	94^{+54}_{-26}	1	(d),(b)
S5 2116+81	0.086	44.42	< 93	1	(d),(b)
PG 1114+445	0.144	44.6	< 22	2	(e),(a),(b)
NGC 4051	0.002	40.68	< 381	2	(e),(a),(b)
PG 1202+281	0.165	44.39	< 64	2	(e),(a),(b)
NGC 4138	0.003	41.21	< 75	2	(e),(a),(b)
Mrk 766	0.013	42.38	21^{+6}_{-7}	2	(e),(a),(b)
NGC 4258	0.002	40.82	< 284	2	(e),(a),(b)
Mrk 50	0.023	43.19	< 334	2	(e),(a),(b)
NGC 4593	0.009	42.82	< 517	2	(e),(a),(b)
Mrk 1383	0.087	44.17	< 134	2	(e),(a),(b)
NGC 3998	0.0035	41.51	104^{+39}_{-22}	1	(f),(b)
NGC 4579	0.0056	41.9	414^{+146}_{-158}	1	(f),(b)
ESO 103-035	0.013	42.96	100^{+90}_{-30}	1	(g),(b)
IGR 2124	0.02	43.68	80^{+11}_{-9}	1	(g),(b)
B2202-209	0.532	45.22	152^{+103}_{-54}	1	(h),(b)
GRS 1734-292	0.021	43.72	53^{+11}_{-8}	1	(i),(b)

Notes. Col. (1): Source name; Col. (2): Redshift; Col. (3): Logarithm of the 2–10 keV luminosity (erg s^{-1}); Col. (4): High-energy cutoff (keV); Col. (5): telescope flag, 1=*NuSTAR*, 2=nonfocusing; Col. (6): References.

References. (a) Fabian et al. (2015), (b) L19, (c) Malizia et al. (2014), (d) Molina et al. (2019), (e) Vasudevan et al. (2013), (f) Younes et al. (2019), (g) Buisson et al. (2018), (h) Kammoun et al. (2017), (i) Tortosa et al. (2017).

Table A.2: Literature low- z measurements collected in this work

Source	z	$\log L_{2-10}$	E_{cut}	Flag	References
NGC 985	0.043	43.72	< 72	2	(j)
ESO198-G24	0.045	43.8	97^{+312}_{-58}	2	(j)
NGC 1068	0.003	42.26	< 35	2	(j)
3C 120	0.033	44.04	77^{+94}_{-30}	2	(j)
H0557	0.034	43.88	35^{+175}_{-20}	2	(j)
MCG-1-24-12	0.02	42.37	< 420	2	(j)
MCG-5-23-16	0.008	43.11	191^{+110}_{-60}	2	(j)
NGC 3516	0.009	42.83	101^{+404}_{-37}	2	(j)
NGC 4151*	0.003	42.45	56^{+14}_{-10}	2	(j)
NGC 4507	0.012	42.67	152^{+350}_{-70}	2	(j)
NGC 4945	0.002	40.51	122^{+41}_{-26}	2	(j)
Mrk 509*	0.035	43.78	60^{+71}_{-23}	2	(j)
MR 2251	0.068	44.59	132^{+130}_{-68}	2	(j)
NGC 7469	0.017	43.27	211^{+235}_{-95}	2	(j)
Ark 564	0.02468	43.59	46^{+3}_{-3}	1	(k)
MGC +8-11-11	0.0204	43.71	175^{+110}_{-50}	1	(l)
Ark 120	0.033	43.96	180^{+80}_{-40}	1	(l)
PG 1211+143	0.0809	43.54	< 124	1	(l)
1E 0754.6+3928	0.096	43.7	< 170	1	(m)
HE 1143-1810	0.0328	43.74	280^{+170}_{-80}	1	(n)
MCG-01-24-12	0.0196	43.18	70^{+21}_{-14}	1	(o)
PDS 456	0.184	44.97	51^{+4}_{-3}	1	(p)
1RXSJ034704.9	0.095	42.72	$29^{+43.7}_{-18}$	1	(q)
1RXS J174538.1	0.111	43.75	< 83	1	(q)
1RXS J213445.2	0.067	43.24	< 85	1	(q)
2MASS J19334715	0.057	43.39	< 166	1	(q)
2MASX J04372814	0.053	42.85	< 114	1	(q)
2MASX J12313717	0.028	42.34	< 84	1	(q)
2MASX J15144217	0.068	43.19	< 32	1	(q)
2MASX J15295830	0.104	43.5	< 119	1	(q)
2MASX J19301380	0.063	43.66	23^{+29}_{-9}	1	(q)
2MASX J19380437	0.04	42.85	< 105	1	(q)
2MASX J20005575	0.037	42.8	< 207	1	(q)
3C 227	0.086	43.65	< 44	1	(q)
4C +18.51	0.186	43.79	< 55	1	(q)
ESO 438-G009	0.024	42.03	< 140	1	(q)
Fairall 1146	0.031	42.81	< 184	1	(q)
Fairall 1203	0.058	42.75	< 108	1	(q)
[HB89] 0241+622	0.044	43.36	< 211	1	(q)
IGR J14471-6414	0.053	42.75	< 73	1	(q)
IGR J14552-5133	0.016	41.89	< 180	1	(q)
IRAS 04392-2713	0.084	43.46	< 71	1	(q)
LCRSB 232242.2	0.036	41.95	< 51	1	(q)
Mrk 9	0.04	42.34	< 193	1	(q)
Mrk 376	0.056	42.83	< 152	1	(q)
Mrk 595	0.027	41.96	< 67	1	(q)
Mrk 732	0.029	42.5	< 173	1	(q)
Mrk 739	0.03	42.32	< 143	1	(q)
Mrk 813	0.11	43.71	< 177	1	(q)
Mrk 817	0.031	42.56	< 230	1	(q)
Mrk 841	0.036	43.05	< 179	1	(q)
Mrk 1018	0.042	42.18	< 212	1	(q)
Mrk 1044	0.016	42.02	< 214	1	(q)
Mrk 1310	0.019	42.17	< 130	1	(q)
Mrk 1393	0.054	42.48	< 19	1	(q)
NGC 0985	0.043	43.02	< 121	1	(q)
PG 0804+761	0.1	43.56	< 183	1	(q)
PKS 0558-504	0.137	44.03	< 134	1	(q)
RBS 0295	0.074	43.17	< 49	1	(q)

continued.

Source	z	$\log L_{2-10}$	E_{cut}	Flag	References
RBS 0770	0.032	43.05	< 267	1	(q)
RBS 1037	0.084	43.14	< 92	1	(q)
RBS 1125	0.063	42.91	< 98	1	(q)
SBS 1136+594	0.06	43.28	< 92	1	(q)
SDSS J104326.47	0.048	42.67	< 34	1	(q)
UM 614	0.033	42.58	< 106	1	(q)
WKK 1263	0.024	42.94	< 224	1	(q)
NGC 262	0.015	43.62	170^{+40}_{-30}	1	(r)
ESO 195-IG021	0.0494	43.76	< 230	1	(r)
NGC 454 E	0.0121	42.43	< 50	1	(r)
NGC 513	0.0195	42.73	< 230	1	(r)
NGC 612	0.0298	43.82	< 120	1	(r)
2MASX J0140	0.0716	44.0	70^{+40}_{-20}	1	(r)
MCG-01-05-047	0.0172	42.9	< 100	1	(r)
NGC 788	0.0136	43.18	< 100	1	(r)
ESO 416-G002	0.0591	43.53	< 480	1	(r)
NGC 1052	0.005	41.9	80^{+40}_{-20}	1	(r)
2MFGC 2280	0.0152	43.33	< 50	1	(r)
NGC 1229	0.0363	42.93	< 82	1	(r)
NGC 1365	0.0055	42.0	290^{+200}_{-100}	1	(r)
2MASX J0356	0.0748	43.87	< 240	1	(r)
3C 105	0.089	44.36	< 70	1	(r)
2MASX J0423	0.045	44.05	70^{+40}_{-30}	1	(r)
MCG+03-13-001	0.0154	42.63	< 60	1	(r)
CGCG 420-015	0.0294	43.48	< 100	1	(r)
ESO 033-G002	0.0181	42.93	< 460	1	(r)
LEDA 178130	0.035	44.0	< 200	1	(r)
2MASX J0508	0.0175	42.99	160^{+200}_{-60}	1	(r)
NGC 2110	0.0078	43.73	300^{+50}_{-30}	1	(r)
ESO 005-G004	0.0062	42.03	< 140	1	(r)
Mrk 3	0.0135	43.83	150^{+60}_{-30}	1	(r)
ESO 121-IG028	0.0405	43.63	< 150	1	(r)
LEDA 549777	0.061	43.63	< 90	1	(r)
LEDA 511628	0.0469	43.53	90^{+80}_{-30}	1	(r)
MCG+06-16-028	0.0157	42.93	< 110	1	(r)
IRAS 07378-3136	0.0258	43.23	60^{+40}_{-20}	1	(r)
UGC 3995 A	0.0158	42.93	100^{+110}_{-40}	1	(r)
Mrk 1210	0.0135	42.93	90^{+40}_{-20}	1	(r)
MCG-01-22-006	0.0218	43.43	110^{+60}_{-30}	1	(r)
CGCG 150-014	0.0647	43.93	< 110	1	(r)
MCG+11-11-032	0.0363	43.63	< 140	1	(r)
2MASX J0903	0.091	43.73	< 270	1	(r)
2MASX J0911	0.0268	43.33	70^{+60}_{-20}	1	(r)
IC 2461	0.0075	41.93	< 110	1	(r)
MCG-01-24-012	0.0196	43.46	110^{+50}_{-30}	1	(r)
2MASX J0923	0.0424	43.83	40^{+90}_{-20}	1	(r)
NGC 2992	0.0077	43.03	< 380	1	(r)
NGC 3079	0.0037	42.73	40^{+20}_{-10}	1	(r)
ESO 263-G013	0.0335	43.73	< 120	1	(r)
NGC 3281	0.0107	42.53	70^{+10}_{-10}	1	(r)
MCG+12-10-067	0.0336	43.13	< 109	1	(r)
MCG+06-24-008	0.0259	42.92	< 170	1	(r)
UGC 5881	0.0206	42.53	80^{+120}_{-30}	1	(r)
NGC 3393	0.0125	43.53	< 60	1	(r)
2MASX J1136	0.014	42.33	< 350	1	(r)
NGC 3822	0.0209	42.53	< 70	1	(r)
B2 1204+34	0.0791	44.09	< 280	1	(r)
IRAS 12074-4619	0.0315	42.93	< 320	1	(r)
WAS 49	0.061	43.73	60^{+60}_{-20}	1	(r)

continued.

Source	z	$\log L_{2-10}$	E_{cut}	Flag	References
NGC 4388	0.0084	42.87	210^{+120}_{-40}	1	(r)
NGC 4395	0.0011	40.63	120^{+50}_{-30}	1	(r)
LEDA 170194	0.0367	43.2	< 230	1	(r)
NGC 4941	0.0037	41.73	< 50	1	(r)
NGC 4992	0.0251	43.46	80^{+90}_{-30}	1	(r)
Mrk 248	0.0366	43.53	50^{+20}_{-10}	1	(r)
ESO 509-IG066	0.0446	43.63	70^{+50}_{-20}	1	(r)
NGC 5252	0.023	43.43	330^{+150}_{-100}	1	(r)
2MASX J1410	0.0339	42.93	< 80	1	(r)
NGC 5643	0.004	41.13	< 130	1	(r)
NGC 5674	0.0249	43.23	< 100	1	(r)
NGC 5728	0.0094	43.23	80^{+30}_{-20}	1	(r)
IC 4518A	0.0163	42.73	120^{+150}_{-50}	1	(r)
2MASX J1506	0.0377	42.93	< 140	1	(r)
NGC 5899	0.0086	42.23	< 340	1	(r)
MCG+11-19-006	0.044	43.43	< 60	1	(r)
MCG-01-40-001	0.0227	42.93	< 130	1	(r)
NGC 5995	0.0252	43.28	< 340	1	(r)
MCG+14-08-004	0.0239	42.81	< 120	1	(r)
Mrk 1498	0.0547	44.22	60^{+10}_{-10}	1	(r)
IRAS 16288+3929	0.0306	43.37	< 60	1	(r)
NGC 6240	0.0245	44.02	90^{+70}_{-30}	1	(r)
NGC 6300	0.0037	42.04	210^{+100}_{-50}	1	(r)
MCG+07-37-031	0.0412	43.85	< 110	1	(r)
2MASX J1824	0.067	43.83	< 110	1	(r)
IC 4709	0.0169	42.83	140^{+200}_{-60}	1	(r)
LEDA 3097193	0.022	43.34	130^{+110}_{-40}	1	(r)
ESO 103-G035	0.0133	43.25	100^{+20}_{-10}	1	(r)
ESO 231-G026	0.0625	44.12	< 250	1	(r)
2MASX J1926	0.071	43.33	< 70	1	(r)
2MASX J1947	0.0539	43.83	120^{+110}_{-40}	1	(r)
3C 403	0.059	44.03	< 110	1	(r)
2MASX J2006	0.043	43.33	< 80	1	(r)
2MASX J2018	0.0144	42.83	< 100	1	(r)
2MASX J2021	0.017	42.63	< 90	1	(r)
NGC 6921	0.0145	43.13	< 100	1	(r)
MCG+04-48-002	0.0139	42.73	< 150	1	(r)
IC 5063	0.0114	43.03	< 130	1	(r)
NGC 7130	0.0162	43.53	< 100	1	(r)
MCG+06-49-019	0.0213	42.13	< 200	1	(r)
NGC 7319	0.0225	42.63	< 220	1	(r)
NGC 7582	0.0053	41.78	200^{+190}_{-80}	1	(r)
2MASX J2330	0.037	43.13	< 70	1	(r)
PKS 2331-240	0.0477	43.86	< 110	1	(r)
PKS 2356-61	0.0963	44.23	< 80	1	(r)

Notes. Col. (1): Source name; Col. (2): Redshift; Col. (3): Logarithm of the 2–10 keV luminosity (erg s^{-1}); Col. (4): High-energy cutoff (keV); Col. (5): telescope flag, 1=*NuSTAR*, 2=nonfocusing; Col. (6): References. *: AGN with multiple observations in [Dadina \(2007\)](#). Observation dates of selected measurement: 1996-12-06 for NGC 4151, 2000-11-08 for Mrk 509.

References. (j) [Dadina \(2007\)](#), (k) [Kara et al. \(2017\)](#), (l) [Tortosa et al. \(2018\)](#), (m) [Middei et al. \(2020\)](#), (n) [Ursini et al. \(2020\)](#), (o) [Middei et al. \(2021\)](#), (p) [Reeves et al. \(2021\)](#), (q) [Kamraj et al. \(2018\)](#), (r) [Baloković et al. \(2020\)](#).

Table A.3: High- z measurements

Source	z	$\log L_{2-10}$	E_{cut}	Flag	References
2MASSJ16	1.86	45.93	107^{+102}_{-37}	1	(b)
B1422	3.62	45.5	66^{+17}_{-12}	1	(b)
APM 08279	3.91	45.8	99^{+91}_{-35}	1	This work

Notes. Col. (1): Source name; Col. (2): Redshift; Col. (3): Logarithm of the 2–10 keV luminosity (erg s^{-1}); Col. (4): High-energy cutoff (keV); Col. (5): telescope flag, 1=*NuSTAR*, 2=nonfocusing; Col. (6): References.

References. (b) [L19](#).